Physics of Fluids

RESEARCH ARTICLE | AUGUST 21 2025

Tailored control of evaporation flux for uniform coffee-ring patterns in multiple nanofluid droplets

Jinghao Jin (김정호) ; Hyung Ju Lee (이형주) ; Hyoungsoon Lee (이형순) ;
Chang Kyoung Choi (최창경) ; Seong Hyuk Lee (이성혁)

Physics of Fluids 37, 082133 (2025)
https://doi.org/10.1063/5.0278740

Physics of Fluids ARTICLE pubs.aip.org/aip/pof

Tailored control of evaporation flux for uniform coffee-ring patterns in multiple nanofluid droplets

Cite as: Phys. Fluids **37**, 082133 (2025); doi: 10.1063/5.0278740
Submitted: 2 May 2025 · Accepted: 30 July 2025 ·
Published Online: 21 August 2025

Jinghao Jin (김정호),[1] Hyung Ju Lee (이형주),[2] Hyoungsoon Lee (이형순),[1] Chang Kyoung Choi (최창경),[3] and Seong Hyuk Lee (이성혁)[1,a)]

AFFILIATIONS

[1]School of Mechanical Engineering, Chung-Ang University, Seoul 06974, Republic of Korea
[2]Department of Mechanical Engineering, Gangneung-Wonju National University, Wonju-si, Gangwon-do 26403, Republic of Korea
[3]Department of Mechanical and Aerospace Engineering, Michigan Technological University, Houghton, MI 49931, USA

[a)]**Author to whom correspondence should be addressed:** shlee89@cau.ac.kr

ABSTRACT

The present study proposes a straightforward approach to achieving consistent particle deposition patterns in multiple nanofluid droplet evaporation systems by strategically placing de-ionized (DI) water droplets without nanoparticles at both ends of the nanofluid droplet array. A proof-of-concept investigation was conducted through a combination of experimental and numerical analyses for a five-droplet evaporation system, consisting of three nanofluid droplets and two DI water droplets, to control vapor shielding effects. This study also examined contact-line dynamics, vapor concentration distribution, and evaporation flux during the evaporation process. The findings revealed inconsistent coffee-ring patterns formed by the three nanofluid droplets, without the addition of DI water droplets. In contrast, when DI water droplets were placed at both ends of the array, we were able to fabricate nearly consistent coffee-ring patterns. Specifically, the consistency of the coffee-ring patterns improved with an increase in DI water droplet volume, achieved by tailoring the evaporation flux near the droplet edges. Increased DI water volume also extended the total evaporation time due to enhanced vapor accumulation. Moreover, DI water droplets exhibited pinning–depinning behavior during evaporation, whereas nanofluid droplets remained pinned for longer durations as particle aggregation delayed the depinning process.

I. INTRODUCTION

Droplet evaporation involves complicated physical processes, including vapor behavior, contact-line dynamics, internal flow motion, and heterogeneous evaporation rates.[1,2] The droplet evaporation phenomenon has been applied in various industrial applications such as spray cooling, food quality assessment, and medical diagnosis.[3–5] During evaporation, in particular, particle-laden droplets (hereafter referred to as nanofluids) can be utilized to fabricate various deposition patterns, such as coffee-ring, multi-ring, and uniform patterns,[6] which are widely used in practical applications, including surface coating, inkjet printing, and other related fields.[7–9] Generally, particle deposition can be controlled by factors such as liquid composition, particle concentration and size, and substrate wettability.[10–12] During evaporation, the capillary flow forms a coffee-ring pattern, and multi-component droplets exhibit central deposition patterns driven by internal Marangoni flows.[13] Furthermore, the thickness and height of deposition patterns are substantially affected by particle concentration and size.[14,15] Unlike single-droplet systems, multiple-droplet evaporation systems exhibit significantly more complex phenomena. Furthermore, the vapor shielding effect, associated with vapor accumulation between adjacent droplets, changes the local evaporation flux and internal flows, primarily affecting particle deposition patterns.

Physically, the vapor shielding effects can significantly modulate evaporation dynamics by reducing the local evaporation flux and extending overall droplet lifetimes.[16,17] Thus, it is necessary to understand the detailed physics behind the vapor accumulation phenomenon between droplets during evaporation to effectively control the particle deposition pattern. Several researchers[18–20] have demonstrated variations in evaporation time due to the vapor shielding effect, showing that multiple droplet configurations generally exhibit longer evaporation than single-droplet cases. Shaikeea and Basu[18] observed that the evaporation time of paired droplets approached that of a single droplet as the distance between the droplets increased. More recently, Lee *et al.*[19] reported that in a system of three identical droplets arranged in a linear configuration, the droplets at both ends evaporated faster than the droplet at the center. However, as the spacing between droplets

increased, the evaporation times of all three droplets tended to converge. Chong *et al.*[20] numerically simulated nine droplets arranged in a 3×3 grid and found that the droplet in the middle position had the longest evaporation time. Moreover, the vapor accumulation effect is further modulated by factors such as the substrate temperature, surface wettability, and the components of liquids. Hwang *et al.*[21] examined the effect of substrate temperature on vapor accumulation between droplets and found that natural convection suppressed vapor accumulation as the substrate temperature increased. Jin *et al.*[22] performed surface plasmon resonance imaging and numerical simulations on a pair of unary and binary droplets. Their results showed that the presence of a de-ionized (DI) water droplet led to a local change in ethanol concentration within the adjacent ethanol–water mixture droplet, due to vapor accumulation. This accumulation reduced the local evaporation rate of water in the mixture droplets. Rehman *et al.*[23] proposed an evaporation rate model for multiple droplets incorporating a contact angle function, based on both experimental and numerical investigations. Their results showed that, under identical droplet spacing, the evaporation time ratio (multiple droplets to single droplet) decreased with increasing contact angle. Similarly, Tonini and Cossali[24] introduced the concept of screening coefficients, defined as the ratio between the evaporation rate of a droplet in a multi-droplet evaporation system and that of an isolated droplet, through analytical modeling, and found that these screening coefficients become more pronounced with larger contact angles. The vapor shielding effect on evaporation rate, particle transport, and the resulting deposition patterns is not fully understood. Therefore, more in-depth studies are required to elucidate the mechanisms underlying coffee-ring formation during the simultaneous evaporation of multiple droplets.

Meanwhile, some researchers have attempted to control the evaporation rate along the liquid–air interface in a single-droplet evaporation system. Kajiya *et al.*[25] achieved a uniform evaporation rate by placing a solvent bath inside a chamber, which resulted in consistent evaporation across the droplet surface, yet the coffee ring effect persisted. Similarly, Boulogne *et al.*[26] created a uniform evaporation rate using hydrogel substrates beneath droplets and observed coffee-ring patterns. Deegan *et al.*[27] demonstrated that when the evaporation rate peaks at the droplet apex, the internal flow reverses direction, transporting nanoparticles toward the center. Routh and Russel[28] investigated horizontal drying fronts in thin films, highlighting early concepts of vapor concentration control. Kolegov and Barash[29] reviewed various vapor field manipulation techniques, including the influence of neighboring droplets, to control deposition. More recently, Hegde *et al.*[30] and Hu *et al.*[31] showed that asymmetric vapor exposure induces Marangoni flow and directional particle migration. They suggested that mechanisms beyond evaporation flux distribution, such as capillary-driven flow and particle migration, played crucial roles in deposition pattern formation.[32–34] Some studies have reported that particle deposition patterns are strongly dependent on the distribution of evaporation flux. Pradhan and Panigrahi[32] found that local evaporation rates adjacent to two droplets were lower, resulting in reduced particle deposition in those regions. Hatte *et al.*[33] showed that particles were transported to regions with higher evaporation rates when two droplets evaporated. Pradhan and Panigrahi[34] demonstrated that adjacent droplets influence the evaporation flux on the droplet surface, the internal concentration field, and the internal flow.

Despite these observations, achieving a controlled and consistent coffee-ring pattern in multi-droplet evaporation systems remains a significant challenge. In Fig. 1(a), three nanofluid droplets exhibit nonuniform evaporation fluxes because of the vapor accumulation, which suppresses evaporation between the droplets. In contrast, the highest evaporation flux occurs at the outermost edges, where particles are more likely to deposit on the surface due to the uneven evaporation flux distribution. To generate more consistent coffee-ring patterns, the present study proposes a novel and straightforward approach by strategically placing de-ionized (DI) water droplets of different volumes at both ends of a nanofluid droplet array, as illustrated in Fig. 1(b). These DI water droplets modulate vapor accumulation effects and eventually dry out without contributing to particle deposition. Proof-of-concept experiments in this study were conducted for a five-droplet evaporation system, and the resulting coffee-ring patterns were compared accordingly. Moreover, the evaporation characteristics, closely associated with the observed deposition patterns, were investigated as a function of the volume of DI water droplets. In addition, numerical simulations were performed to analyze vapor distribution, local evaporation fluxes, and internal flow dynamics in the multi-droplet evaporation system.

II. METHODS

A. Experimental details

The five-droplet evaporation system, as shown in Fig. 2, can simultaneously deposit multiple droplets linearly on a slide glass (HSU-0101242, Marienfeld, Germany) using two nanoliter dispensers (PJ-30091E, Biofluidix, Germany): one to dispense three nanofluid droplets with an edge-to-edge spacing of 80 μm, and the other to place DI water droplets at equal distances on both sides of the nanofluid

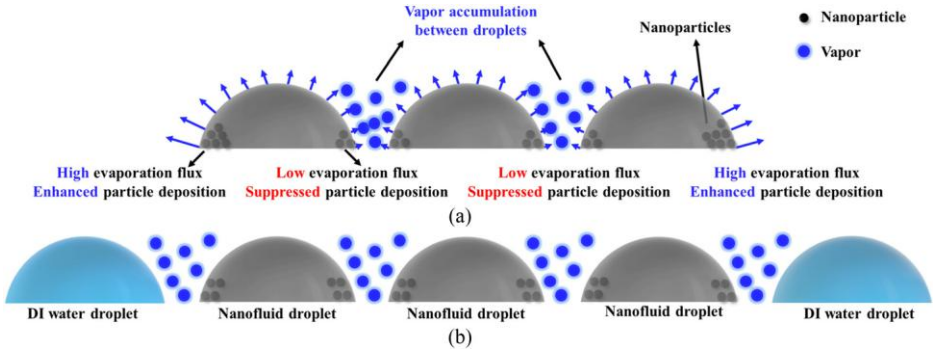

FIG. 1. Schematic of a multiple-droplet evaporation system.

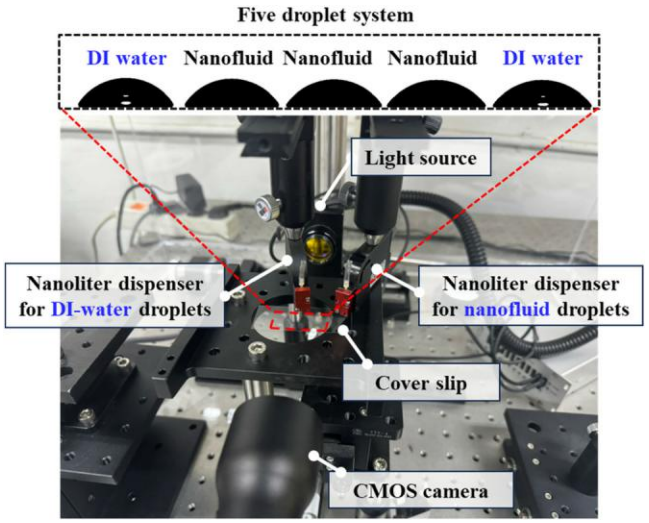

FIG. 2. Experimental setup for the five-droplet evaporation system.

droplet array. In this study, the volume of nanofluid droplets was fixed at 60 nL, whereas the volume of DI water droplets varied at 60, 80, and 100 nL, as listed in Table I.

Visualization of the evaporating droplets was also conducted by using a CMOS camera (ProgRes CT3 USB, JENOPTIK, Germany) equipped with a 1× magnification telecentric lens (1.0× SilverTL™ Telecentric Lens, Edmund Optics, USA), capturing images at one frame per second. Considering the prevalent use of small-sized droplets in printed electronics and particle patterning,[9,35] nanofluid droplets were prepared in this study by mixing 60 nL of DI water with 0.5 wt. % silver nanoparticles (100 nm in diameter, US Research Nanomaterials, USA). Given the small bond number, the droplets were assumed to adopt a spherical cap configuration, indicating that surface forces dominate over gravitational forces. The bond number is defined as follows:

$$Bo = \frac{\rho g R^2}{\gamma}, \tag{1}$$

where ρ is the density of the droplet, g is the gravitational acceleration, R is the radius of the droplet, and γ is the surface tension of the droplet. For DI water droplets with values of 60, 80, and 100 nL, the corresponding bond numbers were calculated to be 0.023, 0.026, and 0.032. For nanofluid droplets containing 0.5 wt. % silver nanoparticles, the measured surface tension was 56.56 ± 0.06 mN/m, resulting in a bond number of 0.028. Therefore, both DI water droplets and nanofluid droplets used in this study can be reasonably assumed to adopt a spherical cap shape.[36] The droplet contact angle and contact diameter were measured using Image J software, with pixel data further processed and analyzed in MATLAB R2019b. The height of the resulting coffee-ring patterns was measured using a three-dimensional (3D) laser microscope (OLS4100-SAA, OLYMPUS, Japan). Each nanofluid droplet had a volume of 60 ± 3 nL, a contact diameter of 0.77 ± 0.05 mm, and a contact angle of 58 ± 4°. DI water droplets of 60 ± 3, 80 ± 3, and 100 ± 4 nL exhibited contact diameters of 0.82 ± 0.03, 0.88 ± 0.05, and 0.97 ± 0.05 mm, and corresponding contact angles of 54 ± 3°, 56 ± 4°, and 54 ± 4°. All experiments were conducted under controlled ambient conditions at a temperature of 22.5 ± 0.3 °C and a relative humidity of 40 ± 2%, with five repetitions performed for each condition to ensure repeatability and data reliability.

TABLE I. Summary of the experimental conditions: case 1 involves three nanofluid droplets without DI water droplets, whereas cases 2–4 correspond to the five-droplet evaporation system in which DI water droplets of varying volumes were placed at both ends of the array.

Case	Number of droplets	Nanofluid droplet volume (nL)	DI water droplet volume
Case 1	3	60	Not used
Case 2	5	60	60 nL
Case 3	5	60	80 nL
Case 4	5	60	100 nL

B. Mathematical representation for computational fluid dynamics (CFD) simulations

For the sake of simplicity, the present study performed numerical simulations of the simultaneous evaporation of five DI water droplets without nanoparticles, aiming to investigate vapor distribution, local evaporation flux, and the corresponding internal flows affected by the vapor shielding effect. Indeed, our simulation aims to demonstrate the feasibility of controlling the evaporation fluxes of droplets through the novel concept proposed in this study. The diffusive timescale (t_D) is given by R^2/D, where R is the droplet radius and D is the diffusion coefficient. This timescale is typically much shorter than the droplet evaporation time, t_e, with $t_D \sim 10^{-5} t_e$. Accordingly, a quasi-steady state assumption is justified for the present numerical simulations.[37,38] For the gas domain, both diffusion and natural convection of water vapor were considered. The evaporation flux at the liquid–air interface was calculated based on Fick's law

$$J = D_v \vec{n} \cdot \nabla c_v, \tag{2}$$

where D_v is the diffusion coefficient, $\vec{n}$ is the normal vector to the liquid–air interface where the liquid is water, the gas is a mixture of water vapor and air, and c is the vapor concentration. This formulation was implemented using a user-defined function (UDF) in ANSYS Fluent (2021-R1) to precisely compute the local interfacial evaporation flux. The liquid–air interface was assumed to be a saturated vapor concentration. The saturated vapor concentration was calculated based on the saturation vapor pressure of water at an ambient temperature of 22.5 °C. The value was determined using the ideal gas law

$$c_{sat} = \frac{M P_{sat}}{RT}, \tag{3}$$

where P_{sat} is the saturation pressure of water at 22.5 °C, approximately 2.73 kPa, M is the molecular weight of water, which is 18 g/mol, R is the universal gas constant, equal to 8.314 J/mol K, and T is the ambient temperature. Substituting the values gives c_{sat} is about 0.02 kg/m^3. The surface tension gradient was applied at the liquid–air interface, considering the thermal Marangoni stress

$$\vec{\tau} = \frac{\partial \gamma}{\partial T} \nabla T, \tag{4}$$

where $\vec{\tau}$ is shear stress, and γ is surface tension. A commercial computational fluid dynamics (CFD) software, ANSYS Fluent (2021-R1), was used to solve the continuity, momentum, energy, and species transport equations, which are expressed as follows:

$$\nabla \cdot (\rho \vec{u}) = 0, \tag{5}$$

$$\nabla \cdot (\rho \vec{u}\vec{u}) = -\nabla p + \mu \nabla^2 \vec{u} + \rho \vec{g}, \tag{6}$$

$$\nabla \cdot (\vec{u}(\rho E + p)) = k\nabla^2 T + S_l, \tag{7}$$

$$\nabla \cdot (\rho \vec{u} Y_i) = \nabla \cdot (\rho D_v \nabla Y_i), \tag{8}$$

where ρ is the density, $\vec{u}$ is the velocity, p is the pressure, μ is the dynamic viscosity, $\vec{g}$ is the gravitational acceleration, E is the total energy, defined as $E = e + 1/2u^2$, with $e = c_v T$, e is the internal energy and c_v is the specific heat, k is the thermal conductivity, T is the temperature, D_v is the diffusivity of water vapor, with a value of 2.5×10^{-5} m^2/s, and Y_i is the mass fraction of each species, namely water vapor and air.[39] The thermophysical properties used in the model are summarized in Table II. The density of the gas phase was calculated using the mixture density formula, expressed as $\rho_{\text{mix}} = 1/\sum_i Y_i/\rho_i$, which depends on the vapor concentration. S_l represents the energy source term applied at the liquid–air interface (i.e., the liquid-side cells adjacent to the interface) to account for evaporative cooling. The energy source term is calculated as $S_l = -h_{fg} J A_c / V_c$, where h_{fg} is the latent heat of vaporization, A_c is the surface area of the computational cell, and V_c denotes the volume of the cell. The pressure–velocity coupling was handled using a coupled scheme, which solves the momentum and continuity equations simultaneously to improve convergence in simulations. Gradient reconstruction was performed using the least squares cell-based method. Second-order upwind schemes were applied for the spatial discretization of momentum, energy, and species transport equations, while the pressure was discretized using a second-order scheme.

TABLE II. Properties of the material.[40]

Property (unit)	Water	Gas phase (Air + Vapor)
Density (kg/m^3), ρ	998.2	Ideal gas law
Viscosity (kg/m s), μ	0.001 003	1.72×10^{-5}
Thermal conductivity (W/m K), k	0.6	0.0454
Specific heat capacity (J/kg K), c_p	4182	Mixing law

Figure 3 illustrates the computational domain measuring $50 \times 50 \times 50$ mm^3. Following previous studies, the domain size exceeded 20R, ensuring that the vapor concentration at the boundaries was equivalent to the ambient vapor concentration to minimize the influence of boundary conditions on the evaporation process.[41] Five droplets were placed on the bottom surface. The computational mesh consisted of tetrahedral elements, with three prism layers applied near the droplet contact-line region to more accurately capture interfacial phenomena. A grid independence test was performed to determine the optimal mesh resolution. In numerical simulations, the evaporation rate was obtained by integrating the evaporation flux over the liquid–air interface. The deviation in the evaporation rate was found to be 0.6% when comparing a mesh system with 3 100 833 cells to the finest mesh system containing 6 591 238 cells. Based on this result, the grid system with 3 100 833 cells was selected when considering both computational efficiency and numerical accuracy.

III. RESULTS AND DISCUSSION

A. Vapor shielding characteristics of the multiple droplets evaporation system

According to a previous study,[21] vapor transport around a droplet at room temperature is primarily governed by diffusion, with the effect of natural convection being negligible compared to diffusion. Figure 4(a) shows predicted vapor distributions for the five-droplet evaporation system in the x–z and x–y planes for the DI water droplet volume of 60 nL. An increase in vapor density between droplets, attributed to the vapor shielding effect, results in a prolonged total evaporation time for complete drying, whereas vapor accumulation along the y-direction remains relatively limited. Figure 4(b) illustrates the predicted spatial distribution of water vapor mass fraction along the line A-A' at $z = 0.3$ mm. The highest water vapor mass fraction is observed at the apexes of the droplets and gradually decreases in the

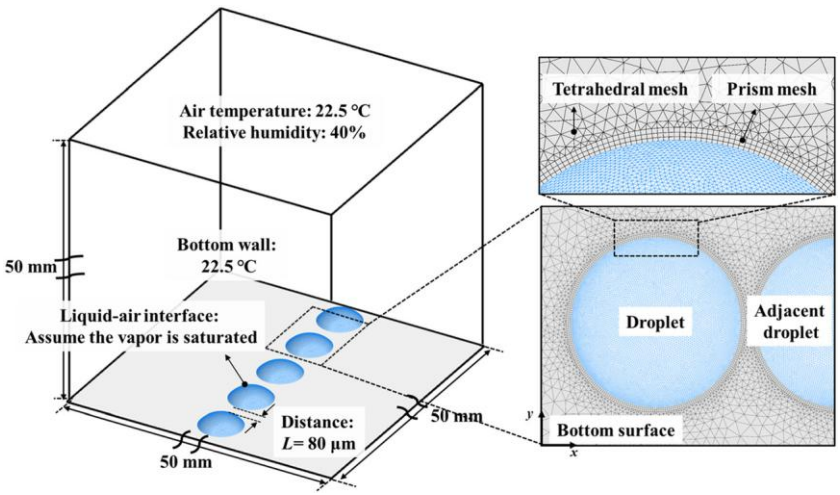

FIG. 3. Computational domain and grid system of the five-droplet evaporation system.

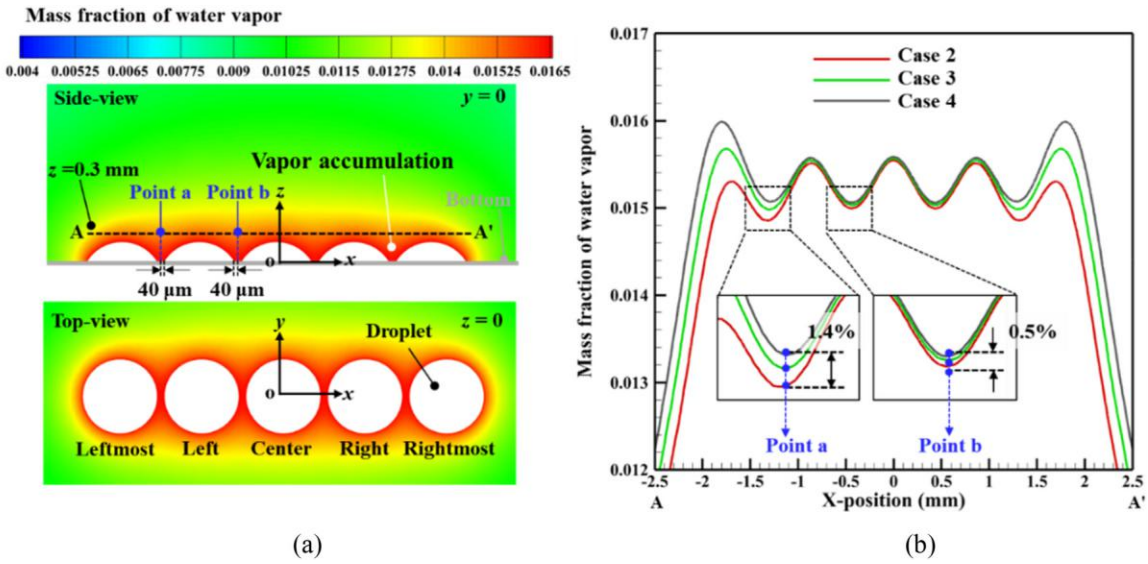

FIG. 4. (a) Simulated vapor distributions (five-droplet case) and (b) water vapor mass fraction at $z = 0.3$ mm.

surrounding regions. As the volume of DI water droplets increases, the surface area of the droplets also increases, resulting in a higher water vapor mass fraction near the leftmost and rightmost droplets.

Meanwhile, variations in DI water droplet volume have little effect on the vapor mass fraction at the apexes of the three droplets between two DI water droplets. For instance, as the DI water droplet volume increases from 60 to 100 nL (cases 2, 3, and 4), the mass fraction of water vapor increases by 1.4% at point a, located 40 μm from the left edge of the left droplet at $z = 0.3$ mm between the leftmost and left droplet, as shown in Fig. 4(a). Additionally, the increase at point b, positioned 40 μm from the right edge of the left droplet between the left and center droplet, is only 0.5%.

Figure 5 presents the normalized evaporation flux along the liquid–air interface in the x-direction for four cases. The normalized evaporation flux is defined as the local evaporation flux divided by the maximum evaporation flux for each case. For the three-droplet evaporation system, the maximum evaporation flux was estimated to be 0.0021 kg/m^{2}s. For the five-droplet evaporation system, the maximum evaporation flux was found to be 0.0017 kg/m^{2}s for the 60 nL case, 0.0016 kg/m^{2}s for the 80 nL case, and 0.0015 kg/m^{2}s for the 100 nL case. Typically, the evaporation flux peaks at the contact line for a single-droplet evaporation system. However, in multiple-droplet evaporation systems, the evaporation fluxes of the droplets are significantly reduced in adjacent regions due to vapor accumulation. In the three-droplet evaporation system (case 1), as illustrated in Fig. 5, the left edge of the left droplet and the right edge of the right droplet exhibit the highest evaporation flux, whereas the evaporation flux at both edges of the center droplet is significantly suppressed by vapor accumulation. This non-uniform evaporation flux distribution leads to inconsistent coffee-ring patterns among the droplets. To resolve this non-uniformity, the present study positioned these pure DI droplets at both ends of the three nanofluid droplets to passively tailor the evaporation fluxes. The DI droplets eventually evaporate completely, leaving behind only three coffee rings with consistent patterns. In Fig. 5, cases 2–4 show that the fluxes of the three central droplets become nearly identical. As the DI water droplet volume increases from 60 to 100 nL, the evaporation flux at the left edge of the left droplet decreases from 0.15 to 0.13 g/m^{2}s, representing a 13% reduction, whereas the evaporation flux at the right edge of the left droplet remains nearly unchanged. With increasing DI water droplet volume, water vapor accumulation between the leftmost droplet and the left droplet is more significantly influenced, whereas the variation in water vapor between the left droplet and the center droplet is comparatively minor, as shown in Fig. 4(b). Therefore, these numerical findings indicate that the additional DI water droplets can effectively control the evaporation fluxes among the droplets.

Generally, the coffee-ring pattern of the droplets is closely associated with their internal flow dynamics. At room temperature, a small temperature gradient along the liquid–air interface occurs, leading to weak thermal Marangoni flow, compared to capillary flow.[39,42] Figure 6 presents the velocity distributions and streamlines at $z = 0.005$ mm for cases 1 and 4 to illustrate the influence of DI water droplets on the internal flows. In case 1, radially outward liquid flow is observed inside the droplets due to the highest evaporation fluxes occurring at both edges of the left and right droplets, whereas the flow inside the center droplet is suppressed by the vapor shielding effects. In contrast, in case 4, where two DI water droplets are placed at both ends, the internal flow within the three central droplets remains nearly uniform, indicating that the DI water droplets can control the evaporation fluxes induced by the vapor shielding effect.

B. Tailored control of evaporation flux for uniform coffee-ring patterns

1. Evaporation characteristics of three-nanofluid-droplet systems

The present study conducted experiments with three 0.5 wt. % silver nanofluid droplets spaced 80 μm apart to evaluate the vapor-shielding effect on evaporation characteristics and coffee-ring

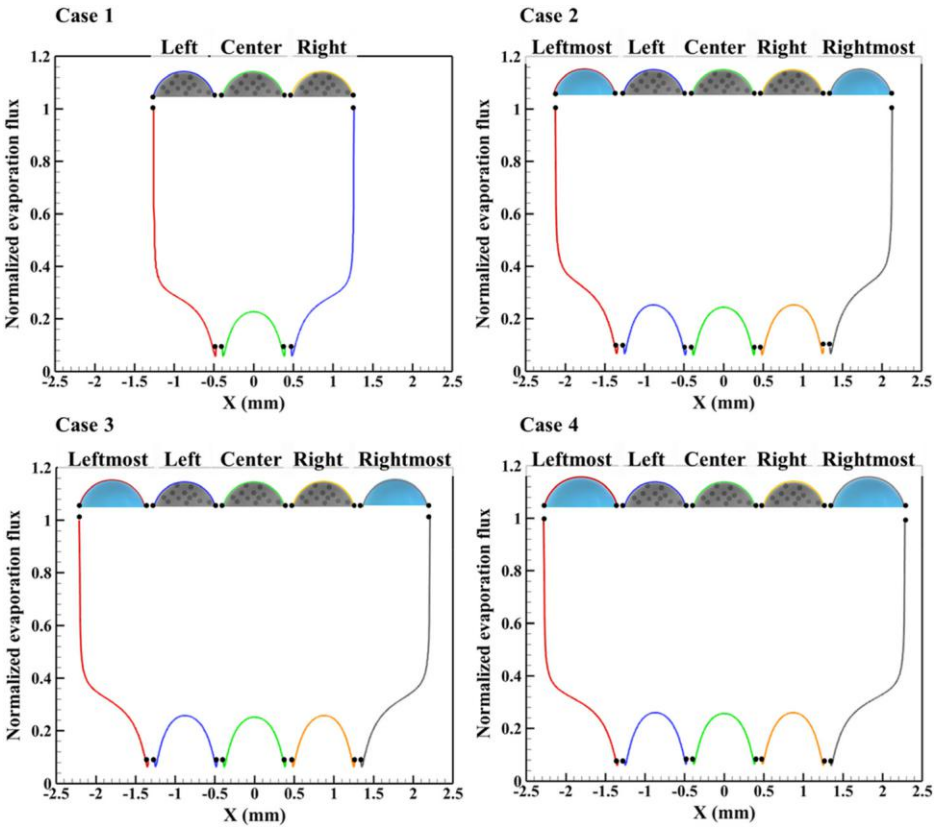

FIG. 5. Evaporation flux distribution of droplets in four cases.

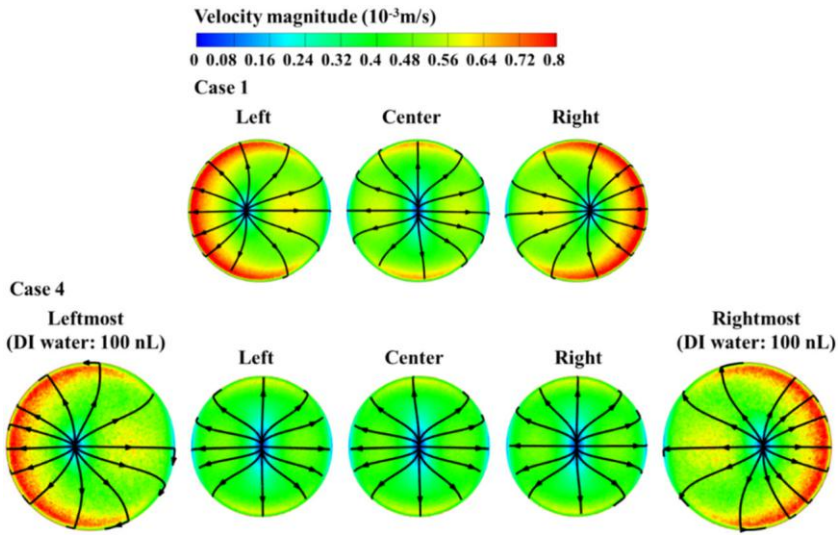

FIG. 6. Velocity magnitude and streamlines at $z = 0.005$ mm for case 1 and case 4.

patterns. Figure 7(a) shows the normalized volume changes, V/V_0, for a three-nanofluid-droplet system during evaporation, with the droplets designated from left to right as the left, center, and right droplets. Droplet volumes are determined under the spherical cap assumption based on experimentally measured contact angles (θ) and contact radius (R_c)

$$V(t) = \frac{\pi R_C^3}{3} \frac{(1-\cos\theta(t))^2(2+\cos\theta(t))}{\sin^3\theta(t)}, \tag{9}$$

where contact radius (R_c) refers to the contact radius at the substrate, defined as half of the measured contact diameter. The center droplet exhibits the longest evaporation time of 218 ± 10 s, while the left and

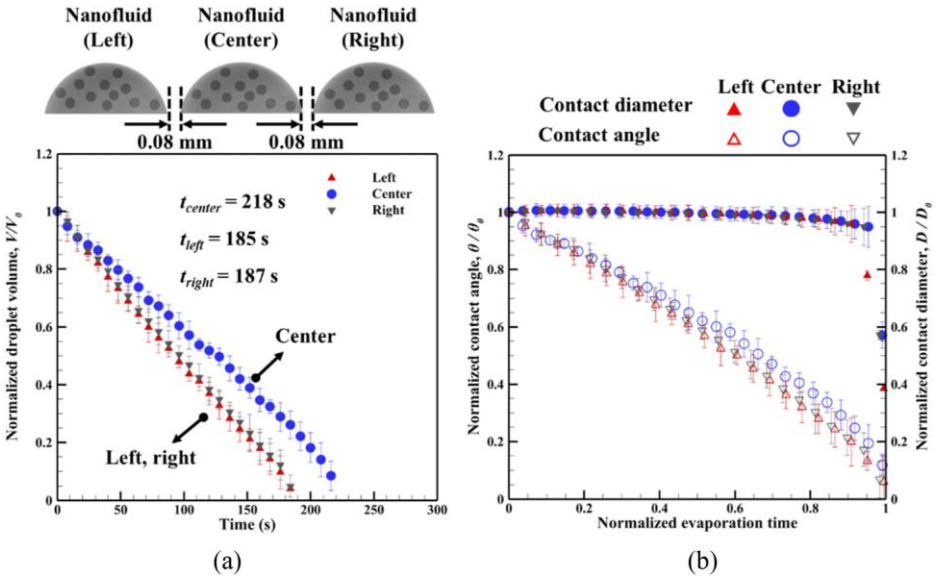

FIG. 7. (a) The droplet volume variation of the evaporating three droplets and (b) the evolution of normalized contact angle and normalized contact diameter of the evaporating three droplets.

right droplets have nearly similar evaporation times of 185 ± 15 and 187 ± 10 s, respectively. In experiments, the total evaporation rate of a droplet is defined as the total initial mass of the droplet divided by the total evaporation time. The total mass of the droplet is calculated based on its volume and density. The total evaporation time is defined as the time at which the droplet disappeared from the side-view image. The evaporation rates of the left, center, and right droplets are $3.3 \pm 0.26 \times 10^{-7}$, $2.8 \pm 0.40 \times 10^{-7}$, and $3.3 \pm 0.36 \times 10^{-7}$ g/s, respectively. The prolonged evaporation time of the center droplet is attributed to vapor accumulation from neighboring droplets, suppressing its evaporation rate compared to the side droplets. Figure 7(b) presents the normalized contact angle (θ/θ_0) and normalized contact diameter (D/D_0) for the three nanofluid droplets during evaporation. In the early stage of evaporation, all three droplets exhibit a pinned stage, maintaining a constant contact diameter while the contact angle gradually decreases. In addition, it shows that the contact diameter begins to shrink as evaporation progresses to approximately 80% of the total evaporation time, indicating that capillary flow drives nanoparticles toward the contact line and the accumulation of particles hinders the depinning process.[43]

2. Evaporation characteristics of five-droplet evaporation systems

The evaporation behavior of the five-droplet evaporation system is examined to clarify the effect of DI water droplet volume on vapor

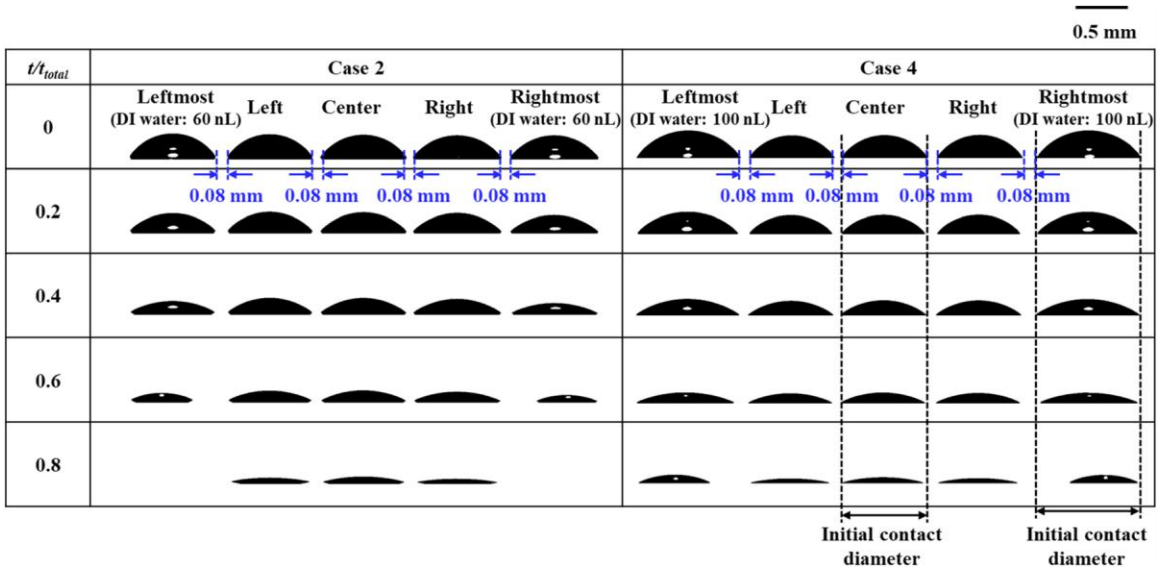

FIG. 8. Side-view images of the evaporating droplet for cases 2 and 4.

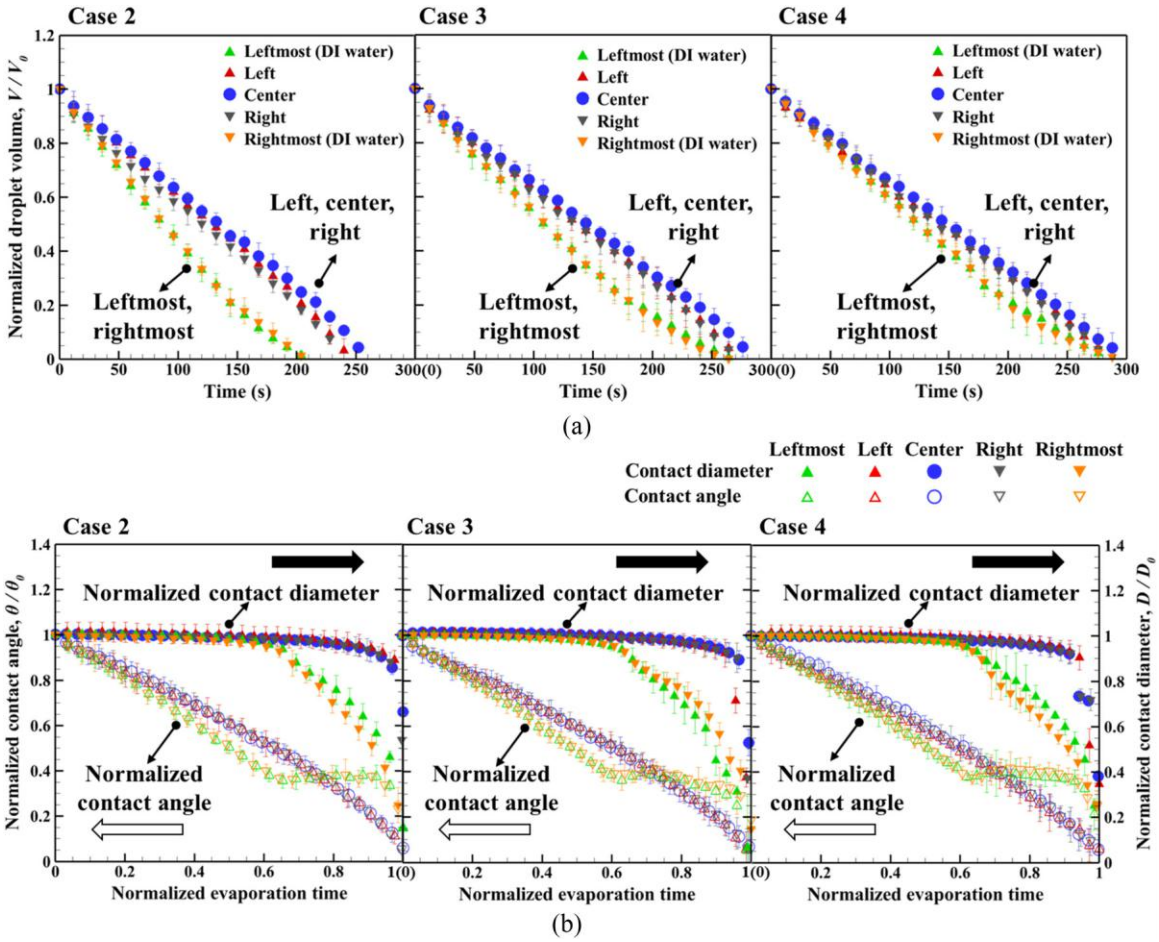

FIG. 9. (a) Droplet volume variation of the evaporating five droplets and (b) normalized contact angle and normalized contact diameter of the evaporating five droplets.

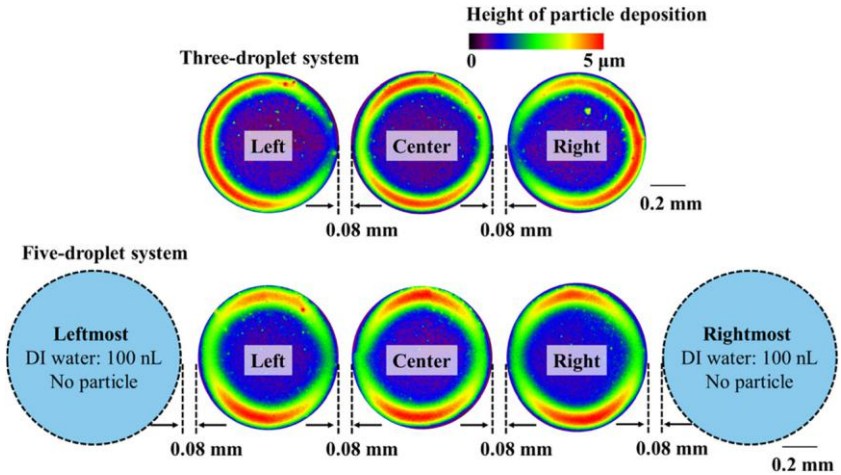

FIG. 10. Coffee-ring pattern observed from a 3D laser microscope for case 1 and case 4.

accumulation. Figure 8 shows side-view images of the evaporation process for cases 2 and 4. When the DI water droplet volume equals the nanofluid droplets (60 nL), the three central droplets exhibit slower evaporation due to significant vapor accumulation than the DI water droplets. As the volume of the DI water droplets increases to 100 nL, the differences in evaporation time among all five droplets become smaller, indicating a more uniform evaporation behavior across the system. Interestingly, the contact diameter of the nanofluid droplets remains nearly unchanged due to strong pinning from particle accumulation at the contact line, whereas the DI water droplets without nanoparticles exhibit the typical pinning–depinning behavior. This result shows the distinct roles of nanoparticles and DI water in affecting contact line behavior and overall evaporation characteristics.

Figure 9(a) delineates the normalized volume changes, V/V_0, for a five-droplet system during evaporation. The total evaporation times observed in case 2, case 3, and case 4 are 256 ± 2, 282 ± 14, and 290 ± 15 s, respectively, corresponding to the evaporation time of the center droplet. The total evaporation time of the five-droplet system increases with the volume of DI water droplets because vapor molecules accumulate much more between droplets. In case 2, the evaporation times of the droplets from leftmost to rightmost are measured to be 208 ± 4, 238 ± 4, 256 ± 4, 241 ± 7, and 211 ± 7 s, respectively. Accordingly, the measured evaporation rates are $2.87 \pm 0.28 \times 10^{-7}$, $2.46 \pm 0.24 \times 10^{-7}$, $2.28 \pm 0.05 \times 10^{-7}$, $2.38 \pm 0.28 \times 10^{-7}$, and $2.82 \pm 0.32 \times 10^{-7}$ g/s. The nanofluid droplet located at the center is affected by vapor accumulation from the neighboring nanofluid droplets on both sides, whereas the leftmost and rightmost DI water droplets evaporate more rapidly at the outer edges, where vapor accumulation does not occur. As shown in case 4, it is interesting to note that when the volume of DI water increases to 100 nL, the evaporation times of the five droplets are measured as 284 ± 19, 280 ± 13, 290 ± 15, 279 ± 13, and 291 ± 13 s. The evaporation rates are found to be $3.40 \pm 0.22 \times 10^{-7}$, $2.13 \pm 0.40 \times 10^{-7}$, $2.07 \pm 0.12 \times 10^{-7}$, $2.22 \pm 0.13 \times 10^{-7}$, and $3.45 \pm 0.24 \times 10^{-7}$ g/s, indicating nearly identical evaporation times for all five droplets, because the enhanced vapor accumulation suppresses the evaporation rates of the smaller droplets, ultimately balancing their evaporation times with those of the larger ones.

Figure 9(b) presents the normalized contact angle, θ/θ_0, and normalized contact diameter, D/D_0, for the five-droplet evaporation system. Similar to the observation in Fig. 8, the DI water droplets exhibit pinning-depinning contact-line behavior. In contrast, the nanofluid droplets demonstrate prolonged pinning due to the enhanced pinning effect of the nanoparticles. The DI water droplets remain in the pinning stage until approximately 65% of the total evaporation time, whereas the three nanofluid droplets sustain this state until around 80% due to particle accumulation at the contact line. Furthermore, variations in DI water droplet volume have no noticeable effect on the contact line behavior of the nanofluid droplets.

3. Comparison of coffee-ring patterns

Figure 10 illustrates the coffee-ring patterns obtained using a 3D laser microscope for cases 1 and 4. Nanoparticles accumulate preferentially in the contact line region, forming a "coffee-ring" pattern due to capillary flow during evaporation in three-droplet (case 1) and five-droplet (case 4) evaporation systems. In case 1, the left droplet shows denser deposition on its left side, while the right droplet exhibits more

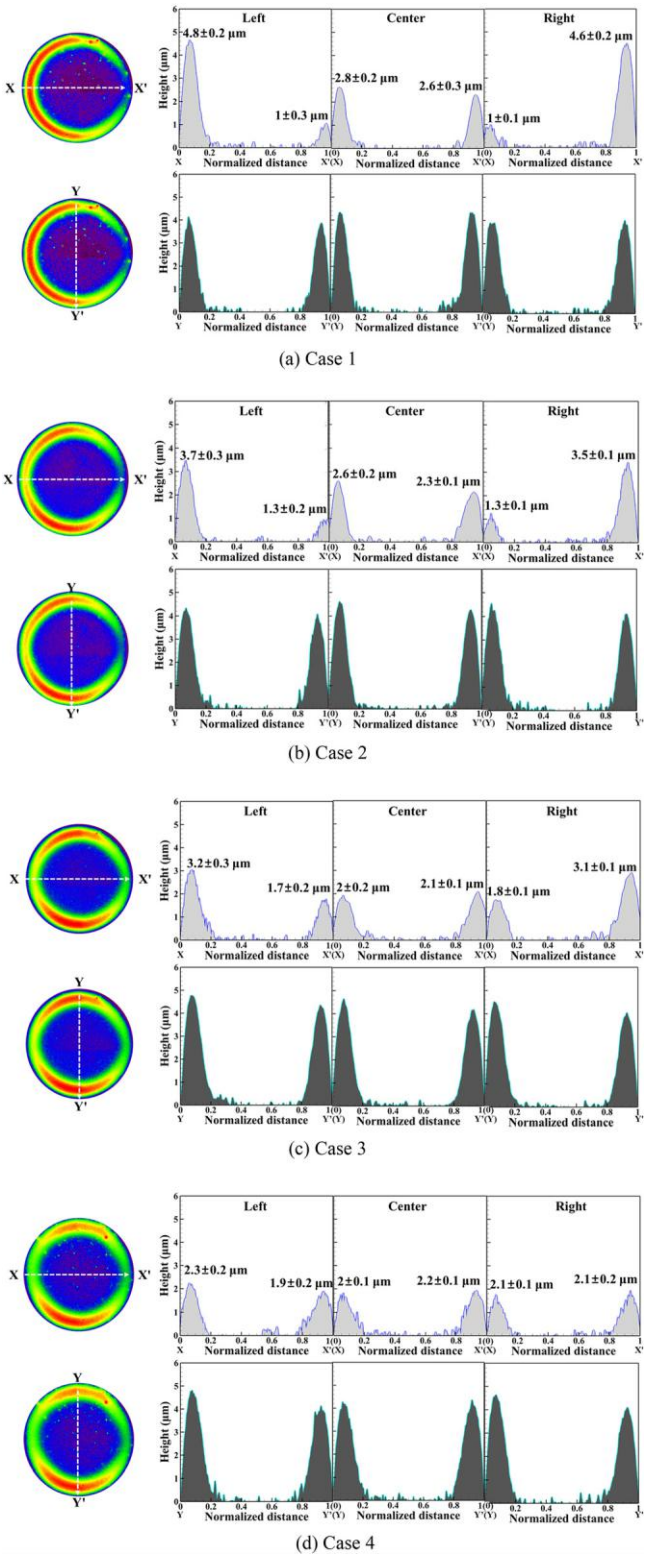

FIG. 11. The measured profiles for particle deposition height.

pronounced deposition on its right side, consistent with previous findings.[32] Moreover, less deposition occurs near the sides adjacent to neighboring droplets due to the vapor shielding effect, whereas increased particle deposition is observed at the top and bottom regions of the center droplet because there are no neighboring droplets in the y direction. This result indicates that the deposition patterns are directly influenced by local variations in evaporation flux caused by vapor accumulation. In case 4, when two DI water droplets of 100 nL are used, the particle concentration in the adjacent regions between the droplets significantly decreases. Compared to case 1, the particle distribution along the x-direction becomes nearly uniform. This result agrees with the CFD analysis, as observed in Fig. 6. On the other hand, more nanoparticles are deposited at the top and bottom ends along the y-direction due to higher local evaporation flux.

Figure 11 quantitatively analyses particle deposition heights along the x- and y-directions. For case 1, the left droplet shows a deposition height of $4.8 \pm 0.2\ \mu$m on its left side and $1 \pm 0.3\ \mu$m on the right side, while the right droplet exhibits an opposite tendency. For the center droplet, due to the nearly symmetric vapor accumulation, only slight differences are observed, measuring $2.8 \pm 0.2\ \mu$m on the left side and $2.6 \pm 0.3\ \mu$m on the right side. In the y-direction, all three droplets exhibit similar particle deposition heights. When DI water droplets of the same volume (60 nL) are placed at both ends, the particle deposition height at the left side of the left droplet decreases to $3.7 \pm 0.3\ \mu$m due to the vapor shielding effect. When the DI water volume is increased to 100 nL, the coffee-ring patterns of the three central droplets become nearly uniform. This result suggests that the vapor accumulation effect becomes more pronounced as the DI water droplet volume increases, gradually reducing the nanoparticle deposition height on the left side of the left droplet. The y-direction profiles consistently show similar deposition heights for all three central droplets, because of negligible effects of vapor accumulation.

The present study compares particle deposition heights measured at six different positions, as illustrated in Fig. 12, to characterize the uniformity. The uniformity of the particle deposition height is defined as

$$U = \left(1 - \frac{\sigma}{\overline{H}}\right) \times 100\%, \tag{10}$$

where σ denotes the standard deviation of the heights measured at six positions for each case, $\overline{H}$ represents the average height measured at six different positions. The height uniformity within the three-droplet array in case 1 is calculated to be approximately 46%. Introducing DI water droplets of equal volume at both ends improves uniformity to 61%. When the volume of the DI water droplets is further increased to 100 nL, the height uniformity markedly increases to 93%, indicating nearly uniform particle deposition across all six measured positions.

IV. CONCLUSIONS

This study suggested a new method for controlling evaporation flux and particle deposition by placing de-ionized (DI) water droplets at both ends of a nanofluid droplet array. The main conclusions are as follows:

(1) Numerical simulations were performed on five DI water droplets without nanoparticles to analyze the evaporation flux and internal flow characteristics that affect particle movements inside droplets. In multiple-droplet evaporation systems, vapor molecules accumulate between them, reducing the local evaporation flux in adjacent regions. Specifically, the internal flow velocity was found to be lower in areas of vapor accumulation.
(2) Based on the insights from the CFD simulation results, the present study conducted the proof-of-concept experiments for the five-droplet configuration, which consisted of three nanofluid droplets of equal volume and two DI water droplets. It was found that the three central nanofluid droplets exhibited an increase in total evaporation time due to vapor accumulation. As the volume of the DI water droplets increased, the vapor shielding effect became more pronounced, increasing the total evaporation time. The DI water droplets also exhibited traditional pinning–depinning behavior during evaporation, whereas the nanofluid droplets maintained a pinned contact line due to the accumulation of nanoparticles near the contact line, which prevented the contact line from moving inward.
(3) In addition, it was experimentally demonstrated that local variations in evaporation flux induced by vapor accumulation resulted in non-uniform coffee-ring patterns. In particular, more uniform and consistent coffee-ring patterns were obtained when two DI water droplets were placed at both ends of the

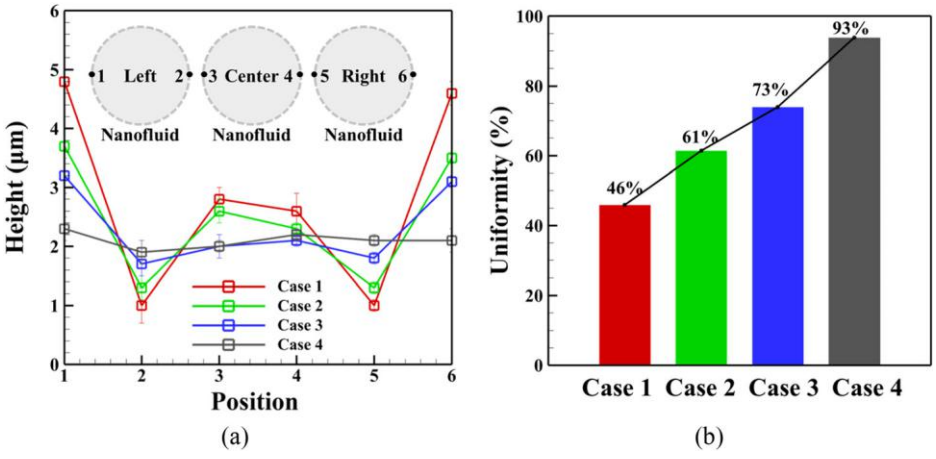

FIG. 12. Comparison of particle deposition heights and uniformity of particle deposition heights.

nanofluid droplet array by tailoring the local evaporation flux. Furthermore, when the volume of each DI water droplet increased to 100 nL, the resulting deposition height in the x-direction became nearly uniform after complete evaporation.

ACKNOWLEDGMENTS

This work was supported by the National Research Foundation of Korea (NRF), Grant funded by the Korea government (MSIT) (No. NRF-2021R1A2C3014510). In addition, this research was supported by the Chung-Ang University Young Scientist Scholarship in 2023.

AUTHOR DECLARATIONS

Conflict of Interest

The authors have no conflicts to disclose.

Author Contributions

Jinghao Jin: Conceptualization (equal); Data curation (lead); Investigation (equal); Methodology (equal); Visualization (lead); Writing – original draft (lead). **Hyung Ju Lee:** Conceptualization (equal); Formal analysis (equal); Investigation (equal); Methodology (equal); Writing – review & editing (equal). **Hyoungsoon Lee:** Conceptualization (equal); Formal analysis (equal); Methodology (equal); Validation (equal); Writing – review & editing (equal). **Chang Kyoung Choi:** Conceptualization (supporting); Formal analysis (supporting); Investigation (supporting); Methodology (equal); Supervision (supporting); Writing – review & editing (equal). **Seong Hyuk Lee:** Conceptualization (equal); Formal analysis (equal); Funding acquisition (equal); Investigation (equal); Methodology (equal); Project administration (equal); Software (equal); Supervision (equal); Validation (equal); Writing – review & editing (equal).

DATA AVAILABILITY

The data that support the findings of this study are available from the corresponding author upon reasonable request.

REFERENCES

[1]D. Zang, S. Tarafdar, Y. Y. Tarasevich, M. Dutta Choudhury, and T. Dutta, "Evaporation of a droplet: From physics to applications," Phys. Rep. **804**, 1 (2019).
[2]M. Parsa, S. Harmand, and K. Sefiane, "Mechanisms of pattern formation from dried sessile drops," Adv. Colloid Interface Sci. **254**, 22 (2018).
[3]J. D. Benther, J. D. Pelaez-Restrepo, C. Stanley, and G. Rosengarten, "Heat transfer during multiple droplet impingement and spray cooling: Review and prospects for enhanced surfaces," Int. J. Heat Mass Transf. **178**, 121587 (2021).
[4]M. O. Kokornaczyk, G. Dinelli, I. Marotti, S. Benedettelli, D. Nani, and L. Betti, "Self-organized crystallization patterns from evaporating droplets of common wheat grain leakages as a potential tool for quality analysis," Sci. World **11**, 1712 (2011).
[5]R. Chen, L. Zhang, D. Zang, and W. Shen, "Understanding desiccation patterns of blood sessile drops," J. Mater. Chem. B **5**, 8991 (2017).
[6]X. Yang, Z. Jiang, P. Lyu, Z. Ding, and X. Man, "Deposition pattern of drying droplets," Commun. Theor. Phys. **73**, 047601 (2021).
[7]H. Kim, F. Boulogne, E. Um, I. Jacobi, E. Button, and H. A. Stone, "Controlled uniform coating from the interplay of Marangoni flows and surface-adsorbed macromolecules," Phys. Rev. Lett. **116**, 124501 (2016).
[8]A. Shimoni, S. Azoubel, and S. Magdassi, "Inkjet printing of flexible high-performance carbon nanotube transparent conductive films by "coffee ring effect"," Nanoscale **6**, 11084 (2014).
[9]M. Layani, M. Gruchko, O. Milo, I. Balberg, D. Azulay, and S. Magdassi, "Transparent conductive coatings by printing coffee ring arrays obtained at room temperature," ACS Nano **3**, 3537 (2009).
[10]S. Lee, A. M. Tiara, G. Cho, and J. Lee, "Control of the drying patterns for complex colloidal solutions and their applications," Nanomaterials **12**, 2600 (2022).
[11]D. Lohani, M. G. Basavaraj, D. K. Satapathy, and S. Sarkar, "Coupled effect of concentration, particle size and substrate morphology on the formation of coffee rings," Colloids Surf., A **589**, 124387 (2020).
[12]M. Yang, D. Chen, J. Hu, X. Zheng, Z.-J. Lin, and H. Zhu, "The application of coffee-ring effect in analytical chemistry," TrAC, Trends Anal. Chem. **157**, 116752 (2022).
[13]J. Pyeon and H. Kim, "Controlling uniform patterns by evaporation of multi-component liquid droplets in a confined geometry," Soft Matter **17**, 3578 (2021).
[14]L. K. Malla, R. Bhardwaj, and A. Neild, "Analysis of profile and morphology of colloidal deposits obtained from evaporating sessile droplets," Colloids Surf., A **567**, 150 (2019).
[15]M. J. Inanlu, B. Shojaan, J. Farhadi, and V. Bazargan, "Effect of particle concentration on surfactant-induced alteration of the contact line deposition in evaporating sessile droplets," Langmuir **37**, 2658 (2021).
[16]X. Man and M. Doi, "Vapor-induced motion of liquid droplets on an inert substrate," Phys. Rev. Lett. **119**, 044502 (2017).
[17]L. Chen and J. R. Evans, "Arched structures created by colloidal droplets as they dry," Langmuir **25**, 11299 (2009).
[18]A. J. Shaikeea and S. Basu, "Insight into the evaporation dynamics of a pair of sessile droplets on a hydrophobic substrate," Langmuir **32**, 1309 (2016).
[19]H. J. Lee, C. K. Choi, and S. H. Lee, "Vapor-shielding effect and evaporation characteristics of multiple droplets," Int. Commun. Heat Mass Transfer **144**, 106789 (2023).
[20]K. L. Chong, Y. Li, C. S. Ng, R. Verzicco, and D. Lohse, "Convection-dominated dissolution for single and multiple immersed sessile droplets," J. Fluid Mech. **892**, A21 (2020).
[21]W. Y. Hwang, H. J. Lee, J. Jin, C. K. Choi, and S. H. Lee, "Enhanced insights into paired droplet evaporation dynamics on heated substrates: Unveiling the role of convection and diffusion," Int. Commun. Heat Mass Transfer **157**, 107740 (2024).
[22]J. Jin, H. J. Lee, L. Li, and S. H. Lee, "Vapor shielding effect and selective evaporation analysis of paired unary and binary mixture droplets using surface plasmon resonance imaging and CFD predictions," J. Mech. Sci. Technol. **38**, 7027 (2024).
[23]M. M. U. Rehman, A. Askounis, and G. Nagayama, "Effect of surface wettability on evaporation rate of droplet array," Phys. Fluids **35**(3), 137614 (2023).
[24]S. Tonini and G. E. Cossali, "Analytical modeling of the evaporation of sessile drop linear arrays," Phys. Rev. E **105**, 054803 (2022).
[25]T. Kajiya, D. Kaneko, and M. Doi, "Dynamical visualization of "coffee stain phenomenon" in droplets of polymer solution via fluorescent microscopy," Langmuir **24**, 12369 (2008).
[26]F. Boulogne, F. Ingremeau, and H. A. Stone, "Coffee-stain growth dynamics on dry and wet surfaces," J. Phys.:Condens. Matter **29**, 074001 (2017).
[27]R. D. Deegan, O. Bakajin, T. F. Dupont, G. Huber, S. R. Nagel, and T. A. Witten, "Contact line deposits in an evaporating drop," Phys. Rev. E **62**, 756 (2000).
[28]A. F. Routh and W. B. Russel, "Horizontal drying fronts during solvent evaporation from latex films," AIChE J. **44**, 2088 (1998).
[29]K. S. Kolegov and L. Y. Barash, "Applying droplets and films in evaporative lithography," Adv. Colloid Interface Sci. **285**, 102271 (2020).
[30]O. Hegde, P. Kabi, S. Agarwal, and S. Basu, "Controlling self-assembly and buckling in nano fluid droplets through vapour mediated interaction of adjacent droplets," J. Colloid Interface Sci. **541**, 348 (2019).
[31]S. Hu, Y. Wang, X. Man, and M. Doi, "Deposition patterns of two neighboring droplets: Onsager variational principle studies," Langmuir **33**, 5965 (2017).
[32]T. K. Pradhan and P. K. Panigrahi, "Deposition pattern of interacting droplets," Colloids Surf., A **482**, 562 (2015).

[33]S. Hatte, K. Pandey, K. Pandey, S. Chakraborty, and S. Basu, "Universal evaporation dynamics of ordered arrays of sessile droplets," J. Fluid Mech. **866**, 61 (2019).
[34]T. K. Pradhan and P. K. Panigrahi, "Influence of an adjacent droplet on fluid convection inside an evaporating droplet of binary mixture," Colloids Surf., A **500**, 154 (2016).
[35]V. Bromberg, S. Ma, and T. J. Singler, "High-resolution inkjet printing of electrically conducting lines of silver nanoparticles by edge-enhanced twin-line deposition," Appl. Phys. Lett. **102**, 214101 (2013).
[36]R. G. Larson, "Transport and deposition patterns in drying sessile droplets," AIChE J. **60**, 1538 (2014).
[37]C. H. Jeong, H. J. Lee, C. K. Choi, and S. H. Lee, "Review of the binary mixture droplet evaporation studies," J. Mech. Sci. Technol. **35**, 5259 (2021).
[38]S. K. Wilson and H.-M. D'Ambrosio, "Evaporation of sessile droplets," Annu. Rev. Fluid Mech. **55**, 481 (2023).
[39]H. J. Lee, C. K. Choi, and S. H. Lee, "Local heating effect on thermal Marangoni flow and heat transfer characteristics of an evaporating droplet," Int. J. Heat Mass Transfer **195**, 123206 (2022).
[40]A. Fluent, *Ansys Fluent Theory Guide* (Ansys Inc., USA, 2011), vol. 15317, p. 724.
[41]H. Hu and R. G. Larson, "Evaporation of a sessile droplet on a substrate," J. Phys. Chem. B **106**, 1334 (2002).
[42]D. Mampallil and H. B. Eral, "A review on suppression and utilization of the coffee-ring effect," Adv. Colloid Interface Sci. **252**, 38 (2018).
[43]P. Katre, S. Balusamy, S. Banerjee, L. D. Chandrala, and K. C. Sahu, "Evaporation dynamics of a sessile droplet of binary mixture laden with nanoparticles," Langmuir **37**, 6311 (2021).